Journal of Zhejiang University-SCIENCE A (Applied Physics & Engineering) *2024 25(12):1037-1050*
www.jzus.zju.edu.cn; www.springer.com/journal/11582
E-mail: jzus_a@zju.edu.cn

Research Article

https://doi.org/10.1631/jzus.A2300455

Check for updates

Mechanical properties of segmental joints strengthened by assembled reinforcement structures for shield tunnel linings

Zhiguo YAN[1,2], Sihang AI[1,2], Xia YANG[3], Long ZHOU[4]✉, Bing FAN[3], Huan PANG[5]

[1]*State Key Laboratory of Disaster Reduction in Civil Engineering, Tongji University, Shanghai 200092, China*
[2]*Department of Geotechnical Engineering, Tongji University, Shanghai 200092, China*
[3]*Jinan Rail Transit Group Co., Ltd., Jinan 250101, China*
[4]*School of Safety Science and Engineering (School of Emergency Management), Nanjing University of Science and Technology, Nanjing 210094, China*
[5]*China Railway No. 5 Engineering Group Co., Ltd., Guiyang 550003, China*

Abstract: We develop assembled reinforcement structures (ARSs) composed of connection parts, connecting rods, and straight bolts to strengthen segmental joints in the lining of shield tunnels. Through full-scale bending experiments and numerical simulations, we investigate the deformation and failure characteristics of segmental joints strengthened by ARSs, and propose a novel optimization method for ARSs. The experimental results show that the ARSs can effectively limit the opening of a segmental joint, but also that separation can occur during loading if the connection between the ARSs and segments is not designed properly. Importantly, this connection can be improved by embedding anchor parts in the concrete. In numerical modeling, we investigate the failure modes of segmental joints strengthened by ARSs for both positive bending and negative bending loading cases. In the case of positive bending loading, first the concrete around the anchor parts cracks, and subsequently the concrete on the external side of the joint is crushed. The joint failure is caused by the crushing of concrete on the external side of the joint. While the un-strengthened segmental joint fails with an opening of 5.884 mm, the strengthened segmental joint only opens by 0.288 mm under the same loading, corresponding to a reduction of 95.1%. In the case of negative bending loading, the concrete around the anchor parts first cracks, and then the amount of joint opening exceeds a limiting value for waterproofing (6 mm), i.e., the joint's failure is caused by water leakage. While the opening of the un-strengthened segmental joint is 9.033 mm and experiences waterproofing failure, the opening of the strengthened segmental joint is only 2.793 mm under the same loading, corresponding to a reduction of 69.1%. When constructing a new shield tunnel, anchor parts could be embedded in the concrete segments in tandem with ARSs for improved resistance to joint opening. For existing shield tunnel linings, anchor parts cannot be embedded in the concrete segments; therefore, the connections between the ARSs and concrete need to be optimized to strengthen the segmental joint.

Key words: Shield tunnel; Segmental joint; Assembled reinforcement structure (ARS); Mechanical properties

1 Introduction

The shield tunneling method has become ubiquitous for the construction of tunnels in urban areas, and is currently used to build highways, railways, subways, and other forms of tunnels (Gong et al., 2015; Zhou et al., 2018). The design service life of shield lining structures is usually about 100 years. Over this long period, material property deterioration and changes in surrounding stratum loads can cause large convergence deformation in the lining rings of shield tunnels, which is often accompanied by issues of joint opening, water leakage, and concrete cracking (Wu et al., 2011; Huang et al., 2017; He et al., 2020; Wang et al., 2023; Ye et al., 2024).

Internal reinforcement technology is an effective method to control the deformation of shield lining rings (Lee and Ishihara, 2010). One common reinforcement strategy is to add steel plates inside the tunnel structure to form a composite system which can improve the structural stiffness and bearing capacity (Liu et al., 2022;

✉ Long ZHOU, zhoulonglmn@126.com
Zhiguo YAN, https://orcid.org/0000-0001-9707-816X

Received Sept. 5, 2023; Revision accepted Mar. 20, 2024;
Crosschecked Nov. 12, 2024

© Zhejiang University Press 2024

Li et al., 2023). In an application of this method, Huang and Zhang (2016) analyzed the measured convergence of a shield tunnel with a large convergence-to-diameter ratio, reinforced the tunnel by gluing steel plates to the inner perimeter of the lining (thus functioning as a secondary lining), and accordingly proposed an acceptable safety level. Further studying the reinforcement of segmental linings, Zhao et al. (2016) proposed an approach based on fiber-beam and discrete elements to model the nonlinear response of a shield lining reinforced with steel plates. Building upon this, Liu et al. (2019) studied the interfacial failure mechanism for the layer between the thin steel plate and tunnel lining, and Zhai et al. (2020) conducted physical tests where deformed segmental tunnel linings were reinforced with steel plates, with the results showing improvements of 190% and 69% in the stiffness and bearing capacity of the tunnel, respectively. In the context of guarding against water leakage, Liu et al. (2020) presented a case study on the structural response of shield tunnel lining rings when unexpected water leakage occurred, and proposed a solution based on reinforcement with steel plates. Furthermore, Zhang et al. (2022) carried out a numerical study in which a tunnel segment was strengthened by steel plates, and proposed that the resulting structural behavior of the segments is governed by the interfacial performance. In addition, Liu et al. (2017) proposed a novel strengthening method for segmental tunnel linings with large deformation, which employs epoxy-bonded filament-wound profiles (FWPs), and used full-scale tests to study the ultimate bearing capacity of deformed segmental tunnel linings strengthened by FWPs. In a similar vein, Liu et al. (2018) investigated the failure mechanism of a shield tunnel structure strengthened by FWPs, with their results showing that the overall failure process is triggered by the failure of concrete at segmental joints.

Shield tunnel linings are usually assembled using prefabricated reinforced concrete segments (Wu and Ou, 2014). Joints are the weakest points in shield lining structures, and thus have a significant impact on the stress and deformation properties of lining structures (Do et al., 2014; Avanaki et al., 2018; Zhou et al., 2023). Previous studies have confirmed that the failure process of shield lining structures exhibits progressive collapse characteristics, and that the failure of tunnel linings typically originates from the failure of joints (Zheng et al., 2017; Zhou et al., 2022). In existing reinforcement technologies, structures such as steel rings are installed around the entire internal side of the lining rings to form a composite structural system. This composite system covers the internal surface of segmental linings and causes difficulties in the observation of water leakage, concrete cracking, and other undesirable effects. Considering how the failure of a shield tunnel usually starts with segmental joint failure, we develop novel assembled reinforcement structures (ARSs) to strengthen the lining joints. ARSs can be installed at joints to restrict the amount of opening and possess the advantage of not covering the lining surface. In this study, full-scale bending experiments were conducted to analyze the mechanical properties of segmental joints strengthened by ARSs, as well as to understand the ARSs' strengthening effect. Then, numerical modeling was performed to understand and account for the weak points in the segmental joint strengthened by ARSs.

2 Full-scale experiment for a segmental joint strengthened by ARSs

2.1 Segmental joint

In this experiment, the lining ring has an outer diameter of 6.4 m, an inner diameter of 5.8 m, a thickness of 0.3 m, and a width of 1.2 m. The lining ring consists of one key segment (K), two adjacent segments (L1 and L2), and three standard segments (A1, A2, and A3). The strength grade of the concrete in the lining is C50. The focus of the experiment is the segmental joint between the standard segments, whose dimensions are shown in Fig. 1. As we were restricted by the size of the loading equipment, two standard segments could not be assembled and placed in the loading equipment; therefore, the size of the joint specimen was reduced accordingly. The reinforcement cage was fabricated according to the size of the adjusted specimen. A steel plate was welded in the mold of a standard segment as shown in Fig. 2a, and then the concrete was cast. After the adjusted segments were demolded, the experimental segments were formed as shown in Fig. 2b. The segments are connected by two curved bolts of Grade 6.8, which have a diameter of 27 mm, a yield strength of 480 MPa, and a Young's modulus of 210 GPa. According to the yield stress and Young's modulus of the bolts, the resulting yield

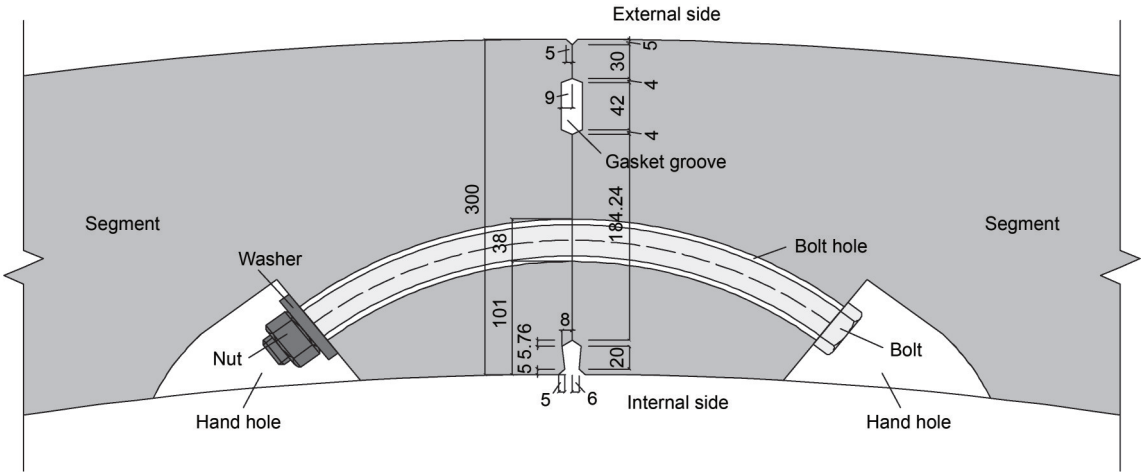

Fig. 1 Dimensions of the segmental joint (unit: mm)

Fig. 2 Segment details: (a) steel mold and reinforcement; (b) segment

strain is 2286 με. Additionally, ethylene-propylene-diene monomer (EPDM) gaskets were put into the gasket groove of the segmental joint.

2.2 ARSs

The ARSs consist of connection parts, connecting rods, and straight bolts, as shown in Fig. 3. The installation process of the ARSs is as follows. First, two connection parts (Fig. 4a) are mounted on the segments at both sides of the joint using eight expansion anchor bolts. Second, two connecting rods (Fig. 4b) are

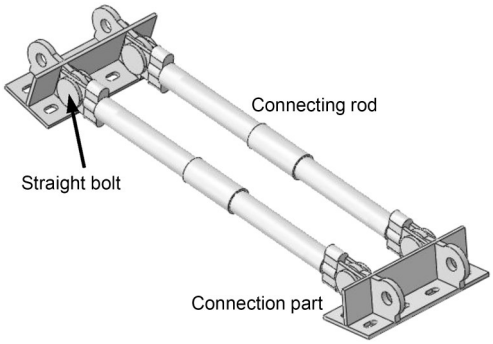

Fig. 3 Schematic diagram of the ARSs

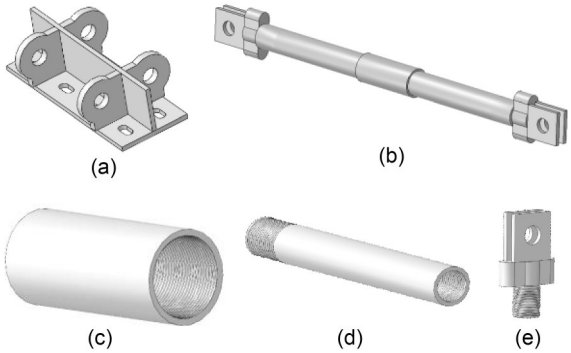

Fig. 4 Details of the ARS components: (a) connection part; (b) connecting rod; (c) sleeve part; (d) rod part; (e) joint part

connected to the two connection parts with four straight bolts. Considering the common types of deformation experienced by segmental joints, such as opening and dislocation over the long-term operation of a tunnel, the connecting rod is made to be adjustable in length. Each connecting rod consists of one sleeve part (Fig. 4c), two rod parts (Fig. 4d), and two joint parts (Fig. 4e). There are also threaded connections between the sleeve part and rod part, and between the rod part and joint part. The installation of ARSs at segmental joints is simple and convenient since ARSs can be easily replaced, and their production components can be standardized. At the same time, ARSs have the advantage of not covering the lining surface after installation, which allows easier observation of problems with the lining.

Considering the structural characteristics of the experimental segmental joint, the design details are as follows. The rod part of the ARSs has an outer diameter of 60 mm, an inner diameter of 48 mm, and a wall thickness of 6 mm; the sleeve part has an outer diameter

of 70 mm, an inner diameter of 60 mm, and a wall thickness of 5 mm; the thickness of the connection part connected to the connecting rod is 16 mm, and the thickness of the other parts is 10 mm. The material of the connecting rods and joint parts is Q345 steel, and the connection between the connecting rod and joint part is made with M36 straight bolts of Grade 6.8. The positive bending experiments were carried out for segmental joints with and without ARSs, so that the reinforcing effect of the ARSs could be determined. The segmental joint system after installation of the ARSs is shown in Fig. 5.

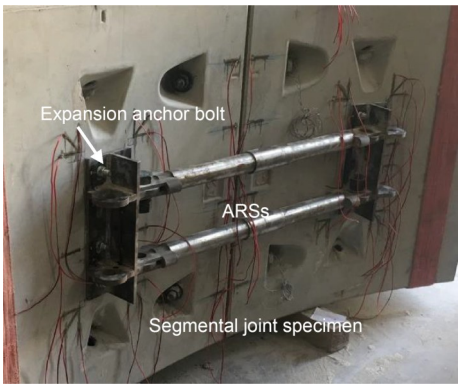

Fig. 5 Segmental joint after installation of ARSs

2.3 Experimental setup

The mechanical behavior and failure modes of a segmental joint subjected to a positive bending moment were investigated. The tests were conducted using a TJ-GPJ2000 loading system at Tongji University, China (Fig. 6a), which enables bi-directional loading of the segmental joint. The TJ-GPJ2000 loading system is comprised of a self-balancing reaction frame, a vertical-loading actuator with a loading capacity of 1500 kN, two horizontal-loading actuators with a loading capacity of 2000 kN, and two loading supports. Positive bending tests were conducted for segmental joints with ARSs (Specimen 1) and without ARSs (Specimen 2). The specimens were placed on the loading system with the external side facing upward and hand holes facing downward, as shown in Fig. 6a. The vertical load P was applied using the vertical actuator, and the horizontal load F was applied using the horizontal actuator. By using the positions of the vertical and horizontal loading actuators and the loading supports in the experimental system shown in Fig. 6b (and ignoring the self-weight of the specimen), the internal

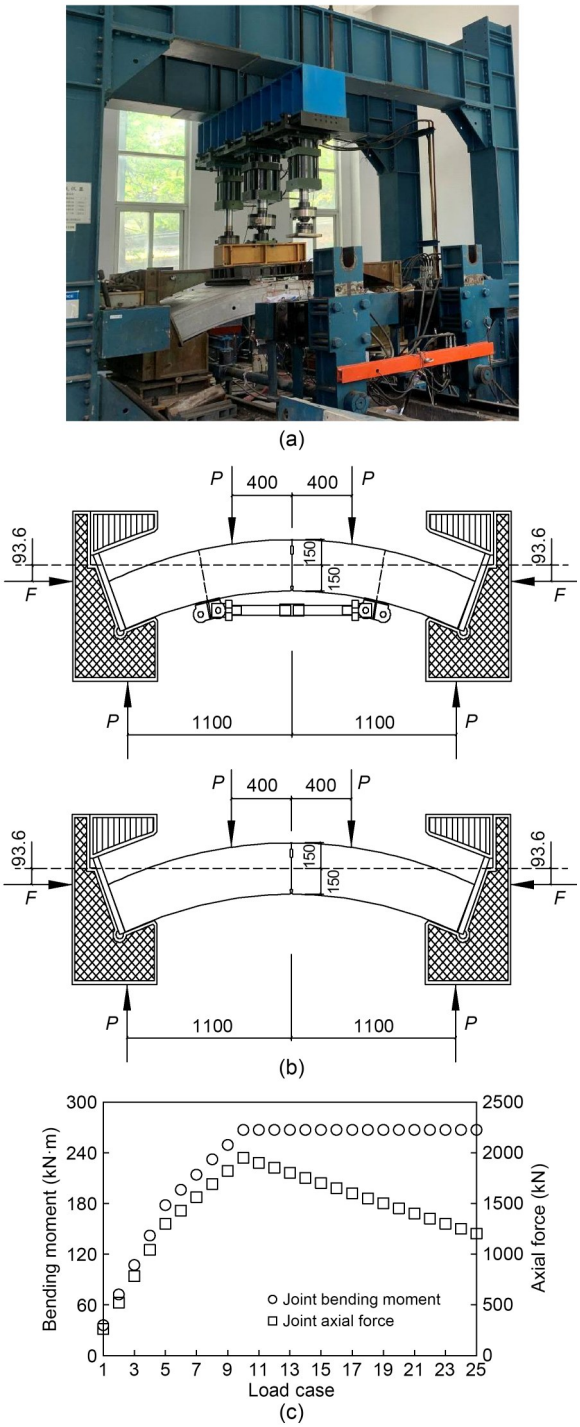

Fig. 6 Test loading: (a) loading equipment; (b) load and displacement boundary conditions (unit: mm); (c) bending moment and axial force at the joint position

force of the joint specimen can be calculated as: M=(0.7 m)×P−(0.0936 m)×F and N=F. The target values of bending moment M and axial force N for the segmental joint specimens were 267 kN·m and 1950 kN,

respectively. During the loading process, the eccentricity ratio e (defined as M/N) was kept constant at 0.14 m (267 kN·m/1950 kN), and the bending moment and axial force at the joint position were increased in 10 equal steps from 0 to 267 kN·m and from 0 to 1950 kN, respectively. After the axial force increased to 1950 kN, an approximate maximum loading capacity of 2000 kN was reached for the horizontal loading actuators. At this point, the bending moment at the joint position was kept constant at 267 kN·m, and the axial force was gradually reduced by 50 kN at each step until the specimen failed. The ultimate limit state, which is where the specimen can no longer support the applied loads and permanently loses its bearing capacity, was adopted as the failure criterion. These loading details are illustrated in Fig. 6c.

In the positive bending test, the internal side of the joint opens and the amount of joint opening is measured by three deformation gauges. A pair of strain gauges utilizing a half-bridge connection was attached to each curved bolt in the segmental joint to measure the strain. This monitoring arrangement is illustrated in Fig. 7. The serial numbers of the measuring points for joint opening and bolt strain in Specimen 1 (with ARSs) are TX1, TX2, and TX3, and TL1 and TL2, respectively. The joint opening and bolt strain measurement methods and locations in Specimen 2 are the same as those in Specimen 1. The serial numbers of the measuring points for joint opening and bolt strain in Specimen 2 (without ARSs) are ZX1, ZX2, and ZX3, and ZL1 and ZL2, respectively.

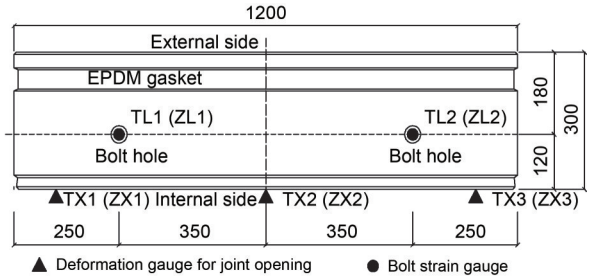

Fig. 7 Monitoring arrangement (unit: mm)

2.4 Experimental results and discussion

2.4.1 Joint opening and bolt strain

The resulting amount of joint opening for the specimens is shown in Fig. 8. Specimen 1 and Specimen 2 are essentially in a closed state from load case 1 to load case 14 (with a bending moment of 267 kN·m and an axial force of 1750 kN). However, after load case 15, the joint specimens gradually open with a decreasing amount of axial force. Looking at load case 17 (which has a bending moment of 267 kN·m and an axial force of 1650 kN), the openings of Specimen 1 and Specimen 2 are 0.96 and 3.26 mm, respectively. Compared with Specimen 2, the opening of Specimen 1 is 70.6% less for the same load case. When the axial force decreases to 1550 kN (load case 18), Specimen 2 (without ARSs) fails with an opening of 5.48 mm, while Specimen 1 (with ARSs) can still bear the positive bending moment with an opening of 1.50 mm. Compared to Specimen 2, the opening of Specimen 1 is 72.6% lower (1.50 mm vs. 5.48 mm). With the bending moment of 267 kN·m held constant, Specimen 1 fails when the axial force decreases to 1250 kN (load case 24) with an opening of 9.39 mm, and the axial force at this failure point is 19.3% lower compared to Specimen 2.

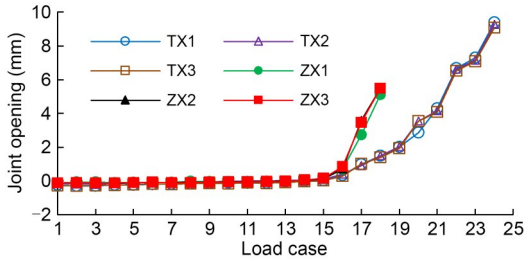

Fig. 8 Segmental joint opening

The strain experienced by the bolts in the specimens is shown in Fig. 9. The bolt strain is effectively 0 from load case 1 to load case 14, because the joint specimens are in a closed state. However, beginning at load case 15, the bolt strain gradually increases with increasing joint opening. Due to the installation of ARSs in Specimen 1, the bolts bear the load together with the ARSs, which results in less joint opening in Specimen 1 than in Specimen 2. Therefore, the strain

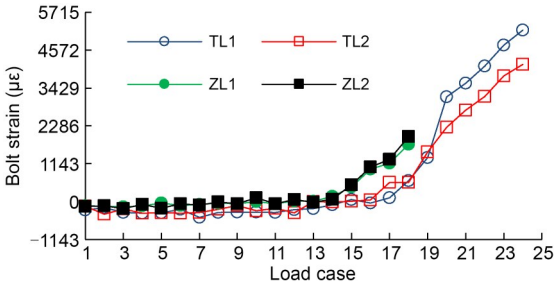

Fig. 9 Joint bolt strain

experienced by the bolts in Specimen 1 is less than in Specimen 2 for the same load case. When the bending moment and axial force are 267 kN·m and 1550 kN, respectively, Specimen 2 fails with an opening of 5.48 mm and a maximum bolt strain of 1961 με, while Specimen 1 can still bear the load with an opening of 1.50 mm and a maximum bolt strain of only 631 με. When the bending moment and axial force are 267 kN·m and 1250 kN, respectively, Specimen 1 fails with an opening of 9.39 mm and a maximum bolt strain of 5180 με.

2.4.2 Joint failure characteristics

The internal and external sides of the joint open and close, respectively, when bearing a positive bending moment and the compressive zone is on the external side of the joint. The concrete in the compressive zone of Specimen 1 cracks in load case 18 (bending moment of 267 kN·m and axial force of 1550 kN) and fails in load case 24 (bending moment of 267 kN·m and axial force of 1250 kN). The concrete in the compressive zone of Specimen 2 cracks in load case 16 (bending moment of 267 kN·m and axial force of 1650 kN) and fails in load case 18 (bending moment of 267 kN·m and axial force of 1550 kN). Both specimens eventually fail because the joint opening cannot be effectively restricted as bearing capacity decreases. The crushing of the concrete in the compressive zone after joint failure is shown in Fig. 10.

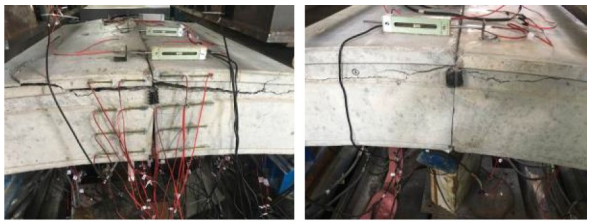

Fig. 10 Concrete crushing on the external side of the segmental joints: (a) Specimen 1; (b) Specimen 2

The security of the connection between ARSs and concrete segments is imperative for strengthening the segmental joint. For Specimen 1 (with ARSs), the connection parts in the ARSs are attached to the concrete surface before loading, as shown in Fig. 11a. When reaching load case 19 (bending moment of 267 kN·m and axial force of 1500 kN), the connection parts start to separate from the concrete surface, as shown in Fig. 11b. Furthermore, the concrete around the connection parts cracks during load case 22 (bending moment of 267 kN·m and axial force of 1350 kN). Finally in load case 24 (bending moment of 267 kN·m and axial force of 1250 kN), the connection parts are pulled out and the concrete around the connection parts is broken, as shown in Fig. 11c. After overall failure, the specimens were removed from the loading system to observe the degree of damage to the concrete on the internal side, as shown in Fig. 12.

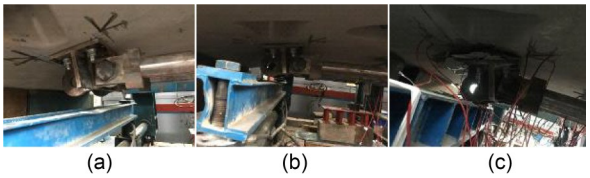

Fig. 11 Failure process of ARSs: (a) contact before loading; (b) separation during loading; (c) pulling out after joint failure

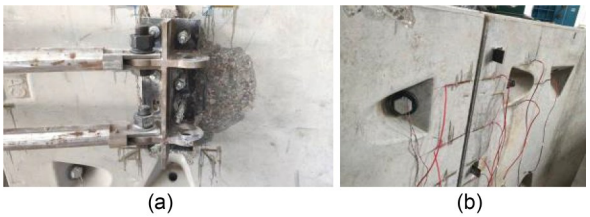

Fig. 12 Comparison of concrete damage on the internal side of the segmental joint: (a) Specimen 1; (b) Specimen 2

Looking at Fig. 12, the concrete on the internal side of Specimen 2 is intact and displays different damage patterns compared to the concrete in Specimen 1. According to the analyses in Section 2.4.1, under the action of a bending moment of 267 kN·m, the axial force failure point for the joint with ARSs is 19.3% lower than the failure point for the joint without ARSs. Additionally, while the joint without ARSs fails with an opening of 5.48 mm, the joint with ARSs only has an opening of 1.50 mm, corresponding to a reduction of 72.6%. Therefore, installing ARSs on the internal side of the segmental joint has a reinforcing effect, restricting the joint opening and improving the ultimate bearing capacity. However, it also results in concrete damage at the ARS connection locations. As a result, it is necessary to optimize the connection between the ARSs and the concrete segments. In Section 3, we propose optimizations to the ARS–concrete connections, and accordingly conduct numerical analyses to analyze the strengthening effect of ARSs after

optimizations on a segmental joint subjected to both positive and negative bending moments.

3 Optimization of the connection between ARSs and concrete segments

3.1 Numerical modeling

In numerical models, anchor parts were used to strengthen the connections between the ARSs and concrete segments, as shown in Fig. 13. The ABAQUS software was used for this numerical modeling. The anchor parts were connected to the connection parts of the ARSs using eight M20 connecting bolts of Grade 6.8, for which the yield strength, Young's modulus, and Poisson's ratio are 480 MPa, 210 GPa, and 0.3, respectively. The dimensions and materials of the ARSs in these numerical models are the same as those in the full-scale bending tests. The connecting rods, joint parts, and anchor parts in the ARSs are all comprised of Q345 steel, for which the yield strength, Young's modulus, and Poisson's ratio are 345 MPa, 210 GPa, and 0.3, respectively. The connecting rod is affixed to the connection part by M36 straight bolts of Grade 6.8, for which the yield strength, Young's modulus, and Poisson's ratio are 480 MPa, 210 GPa, and 0.3, respectively. As simplifying assumptions, only the main reinforcement with a strength grade of HRB400 was considered, and the stirrup was neglected. The yield strength, Young's modulus, and Poisson's ratio of the main reinforcement are 400 MPa, 210 GPa, and 0.3, respectively. This main reinforcement was embedded in the concrete. The strength grade of the concrete is C50, for which Young's modulus and Poisson's ratio are 34.5 GPa and 0.2, respectively. The plastic damage constitutive model was adopted for the concrete, with the resulting compressive and tensile damage behavior of C50 concrete (Jin et al., 2018) shown in Fig. 14.

In the numerical models, surface-to-surface contact was applied for the interactions between the connection parts, connecting rods, and M36 straight bolts. Also, the interactions between the connection parts and anchor parts, as well as those between the anchor

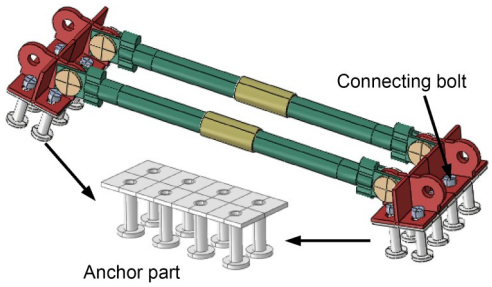

Fig. 13 Optimization of the connections between ARSs and segments

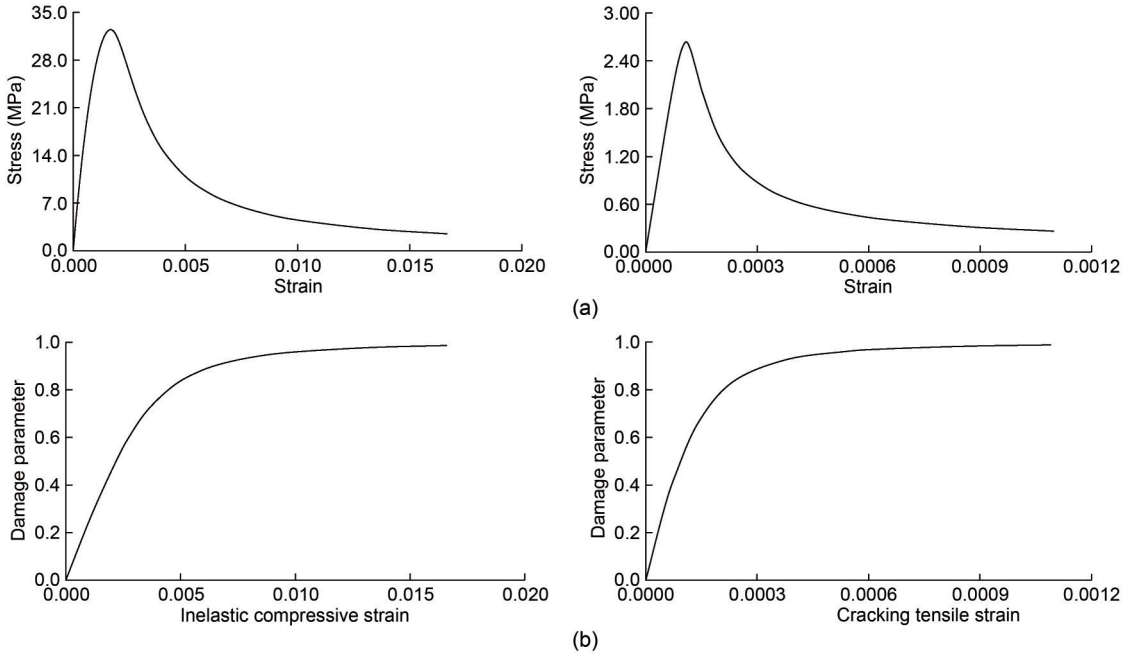

Fig. 14 Plastic damage model for concrete (left: compression; right: tension): (a) stress–strain relation; (b) damage parameter–strain relation

parts and concrete segments, were modeled with surface-to-surface contact. For the bolts used to connect the anchor parts and connection parts, the interfaces between the connecting bolts and connection parts were set to be in surface-to-surface contact, and the connection between the bolts and anchor parts was implemented with the "tie" function in the ABAQUS software. The connection between the sleeve parts and rod parts in the connecting rods was also implemented with the "tie" function. The two segments were connected by two curved M27 bolts of Grade 6.8, which have a Young's modulus of 210 GPa, a yield strength of 480 MPa, and a Poisson's ratio of 0.3. The interactions between the two segments, and between the segments and bolts, were set as surface-to-surface contact. All of the surface-to-surface contact cases above were set as "hard contact" in the normal direction, and "friction contact" (with a friction coefficient of 0.5) in the tangential direction. T3D2 elements were used for the reinforcement parts, and C3D8R elements were used for all the other parts. To simplify the numerical models, EPDM gaskets were not installed at the joint position between concrete segments. The resulting numerical model is illustrated in Fig. 15a. In order to measure the strengthening effect of ARSs, a baseline numerical model of a segmental joint without ARSs was also constructed, as shown in Fig. 15b.

The bending moment M and axial force N at the joint position in the numerical model were applied using a vertical load P and a horizontal load F, as shown in Figs. 16a and 16b. For the positive bending loading mode in Fig. 16a, it can be shown that $M=(0.7\text{ m})\times P-(0.0936\text{ m})\times F$ and $N=F$. For the negative bending loading mode in Fig. 16b, it can be shown that $M=(0.6\text{ m})\times P+(0.07\text{ m})\times F$ and $N=F$. For joints under the action of positive and negative bending moments, the target values for the bending moment M and axial force N were 267 kN·m and 1950 kN, and 186 kN·m and 1640 kN, respectively. In the loading processes for positive and negative bending, the bending moment and axial force were increased in 10 equal steps to the target values, after which the bending moment was increased by 20 kN·m for each step while the axial force was kept constant; this continued until the joint was damaged. The loading details are shown in Figs. 16c and 16d.

There were four groups of numerical models as shown in Table 1. The models with and without ARSs subjected to a positive bending moment are Model 1 and Model 2, respectively; the models with and without ARSs subjected to a negative bending moment are Model 3 and Model 4, respectively.

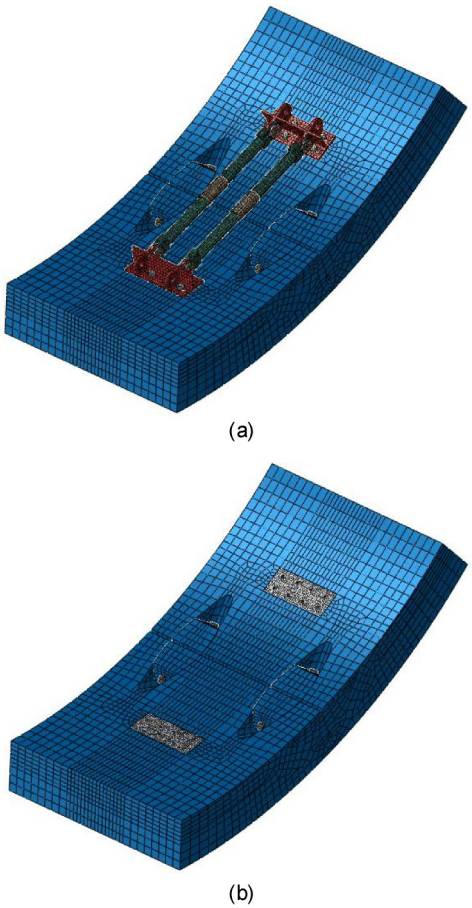

Fig. 15 Numerical models: (a) with ARSs; (b) without ARSs

3.2 Model validation

Model 2 (Fig. 15b) was selected to validate the numerical models, and its loading details are shown in Fig. 6c. The positions of the applied vertical and horizontal loads in the model were the same as those in the bending experiment in Section 2. The position of the joint opening measurement point in Model 2 coincided with that of ZX2 (Fig. 7) in the experiment. The amount of joint opening calculated by the numerical simulation is compared to the experimental result in Fig. 17.

As shown in Fig. 17, the pattern of the joint opening in the numerical simulation follows the experimental results. Both the numerically modeled joint and the real joint begin to open when the bending moment is maintained at 267 kN·m and the axial force decreases

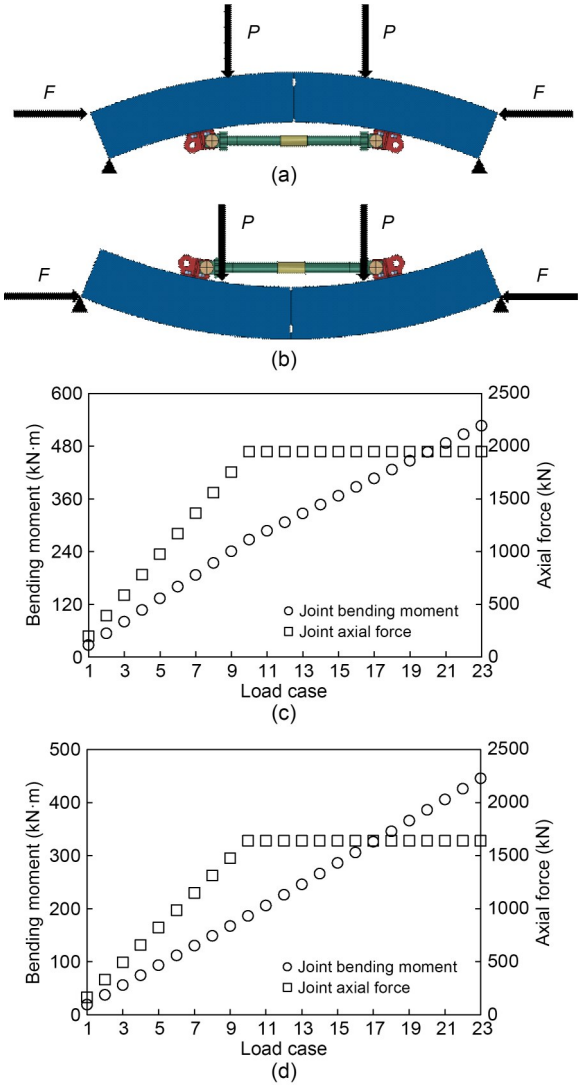

Fig. 16 Loading processes for the numerical simulation: (a) loading mode for positive bending; (b) loading mode for negative bending; (c) bending moment and axial force for positive bending loading; (d) bending moment and axial force for negative bending loading

Table 1 Details of the numerical models

Model	ARS	Loading
1	Yes	Positive bending loading
2	No	Positive bending loading
3	Yes	Negative bending loading
4	No	Negative bending loading

to 1700 kN. The numerically modeled joint fails to bear the load when the axial force is reduced to 1600 kN, corresponding to a difference of only 3.2% from the experimental axial force of 1550 kN. A possible explanation for the difference in joint opening is that the

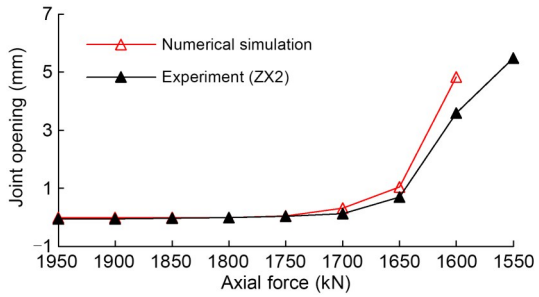

Fig. 17 Comparison of joint opening between numerical and experimental results

EPDM gaskets were not considered in the numerical model. The distribution of the compressive and tensile stresses within the concrete at the time of joint failure is shown in Fig. 18. Note that the compressive and tensile strengths for C50 concrete are 32.4 and 2.64 MPa, respectively. As shown in Fig. 18, the concrete on the external side of the joint experiences stress exceeding the compressive and tensile strengths, thus agreeing with the experimental result shown in Fig. 10b. It should be noted that anchor parts are present in the numerical model (Fig. 15b) but do not bear any load during the loading process because the ARSs are not installed, meaning that the anchor parts have no impact on the stress and deformation properties of the modeled joint. Considering how the characteristics of joint opening and failure for concrete on the external side of the joint agree with experimental results, it is likely that the numerical model reasonably represents the stress and deformation states of the real joint.

3.3 Numerical simulation results and discussion

3.3.1 Joint opening

The waterproofing limit value of the joint in this study is 6 mm, i.e., when the joint opens more than 6 mm, it fails to restrain water. Progressive bending moments and axial forces (Figs. 16c and 16d) were applied for the numerical models from Table 1, until the joints were damaged or the joint opening exceeded the waterproofing limit. Fig. 19 shows the results of these numerical tests, including the joint opening, the maximum value of bolt stress, the maximum value of stress in the ARSs and anchor parts, as well as the maximum value of stress experienced by the connecting bolts between the ARSs and anchor parts.

It is clear from these results that the joint with ARSs opens significantly less than the joint without

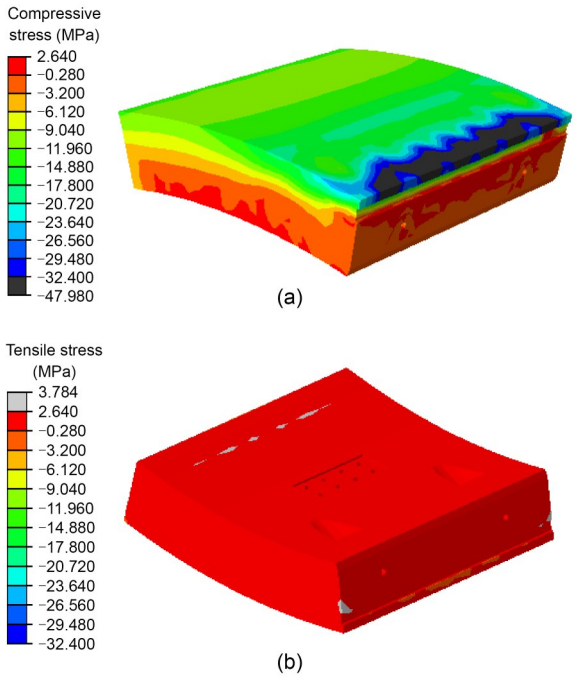

Fig. 18 Concrete stress distribution in the numerical model: (a) compressive stress; (b) tensile stress

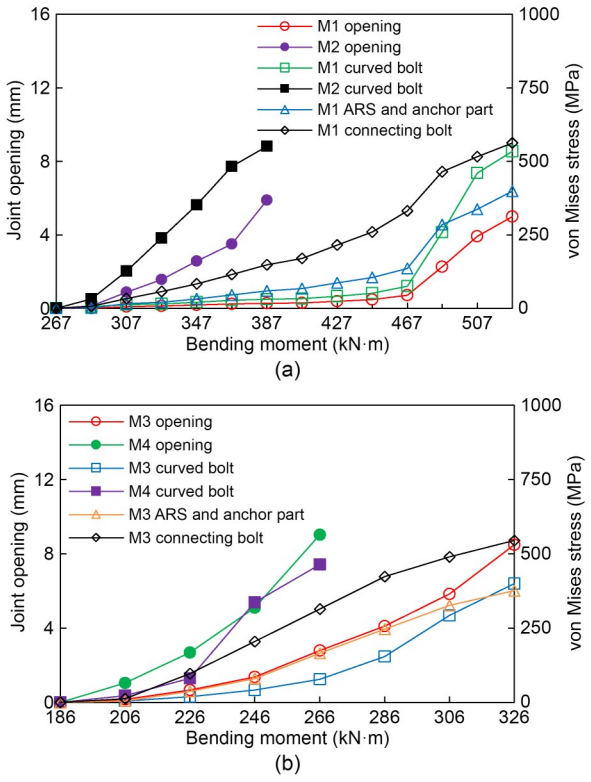

Fig. 19 Joint opening and stresses of bolts, ARSs, and anchor parts (M1, M2, M3, and M4 are Model 1, Model 2, Model 3, and Model 4, respectively): (a) positive bending loading; (b) negative bending loading

ARSs. The joints of Model 1 (with ARSs) and Model 2 (without ARSs) under positive bending moments are damaged in load case 23 and load case 16, respectively. In load case 23, the joint of Model 1 fails at a bending moment of 527 kN·m and an axial force of 1950 kN, with an opening of 4.990 mm. On the other hand, for load case 16, the joint of Model 2 fails at a bending moment of 387 kN·m and an axial force of 1950 kN, with an opening of 5.884 mm. The bending moment failure point in Model 1 is thus 36.2% larger compared to Model 2. Furthermore, compared to the opening of Model 2 (without ARSs) at failure, the opening of Model 1 (with ARSs) is 95.1% lower (0.288 mm vs. 5.884 mm) for the same load case (case 16).

Under the action of a negative bending moment, the joint opening of Model 3 (with ARSs) reaches 8.493 mm with a bending moment of 326 kN·m and an axial force of 1640 kN (load case 17), thus exceeding the limit value of 6 mm. Concordantly, the joint opening of Model 4 (without ARSs) reaches 9.033 mm with a bending moment of 266 kN·m and an axial force of 1640 kN (load case 14), exceeding the limit value as shown in Fig. 19b. When the opening limit value of 6 mm is reached, the bending moment applied on the joint of Model 3 is 22.6% larger compared to Model 4. When the joint opening of Model 4 (without ARSs) reaches 9.033 mm and the waterproofing fails, the joint opening of Model 3 (with ARSs) is 69.1% lower (2.793 mm vs. 9.033 mm) for the same load case (load case 14).

3.3.2 Structure stress and failure characteristics

The joints of Model 1 and Model 2 fail after the crushing of concrete on the external side of the joint, due to the influence of positive bending moments. Fig. 19a shows that the stress of the curved bolts connecting the two segments in both Model 1 and Model 2 exceeds the yield strength of 480 MPa at failure (551.3 and 534.2 MPa for Model 1 and Model 2, respectively). For the joint of Model 1 (with ARSs), the first components to enter the plastic yield state are the connecting bolts between the anchor parts and the ARSs. These connecting bolts yield at load case 22 (bending moment of 507 kN·m and axial force of 1950 kN) with the maximum stress reaching 515.9 MPa (note that the yield strength of the connecting bolts is 480 MPa). In fact, before the connecting bolts yield, the maximum compressive and tensile stresses in the

concrete around the anchor parts exceed the compressive strength of 32.4 MPa and tensile strength of 2.64 MPa for C50 concrete, respectively, at load case 21 (bending moment of 487 kN·m and axial force of 1950 kN). This result is shown in Figs. 20a and 20b, and indicates that the concrete around the anchor parts is the first to be damaged. Since the internal side of the joint opens under a positive bending moment, the ARSs are in a tensional state, which results in the concrete in contact with the anchor parts (close to the hand holes) being damaged by the squeezing of the anchor parts (Fig. 20a). As we reach load case 23 (bending moment of 527 kN·m and axial force of 1950 kN), joint failure occurs due to the crushing of concrete on the external side of the joint, and the curved bolts connecting the two segments, the ARSs, and the anchor parts all enter the plastic yield state. The stress distribution of the concrete, the ARSs, the anchor parts, and the connecting bolts at the point of joint failure is shown in Fig. 21a.

Fig. 19b shows that when subjected to a negative bending moment, the joints of Model 3 (with ARSs) and Model 4 (without ARSs) experience waterproofing failure because the joint opening exceeds the limit value of 6 mm. The stress of the curved bolts connecting the segments does not exceed the yield strength of 480 MPa (400.3 and 463.8 MPa for Model 3 and Model 4, respectively) when water leakage occurs in the joints. For the joint of Model 3 (with ARSs), the connecting bolts between the anchor parts and the ARSs are the first to enter the plastic yield state. The connecting bolts yield at load case 16 (bending moment of 306 kN·m and axial force of 1640 kN) with the maximum stress reaching 490.2 MPa (note that the yield strength of the connecting bolts is 480 MPa). Importantly, before the connecting bolts yield, the maximum compressive stress in the concrete around the anchor parts exceeds the compressive strength of 32.4 MPa for C50 concrete at load case 15 (bending moment of 286 kN·m and axial force of 1640 kN), as shown in Figs. 20c and 20d. This indicates that the concrete around the anchor parts is the first to be damaged in the numerical model. Since the external side of the joint opens under a negative bending moment, the ARSs are in a compression state, which results in the concrete in contact with the anchor parts (away from the hand holes) being damaged by the squeezing of the anchor parts (Fig. 20c). After reaching load case

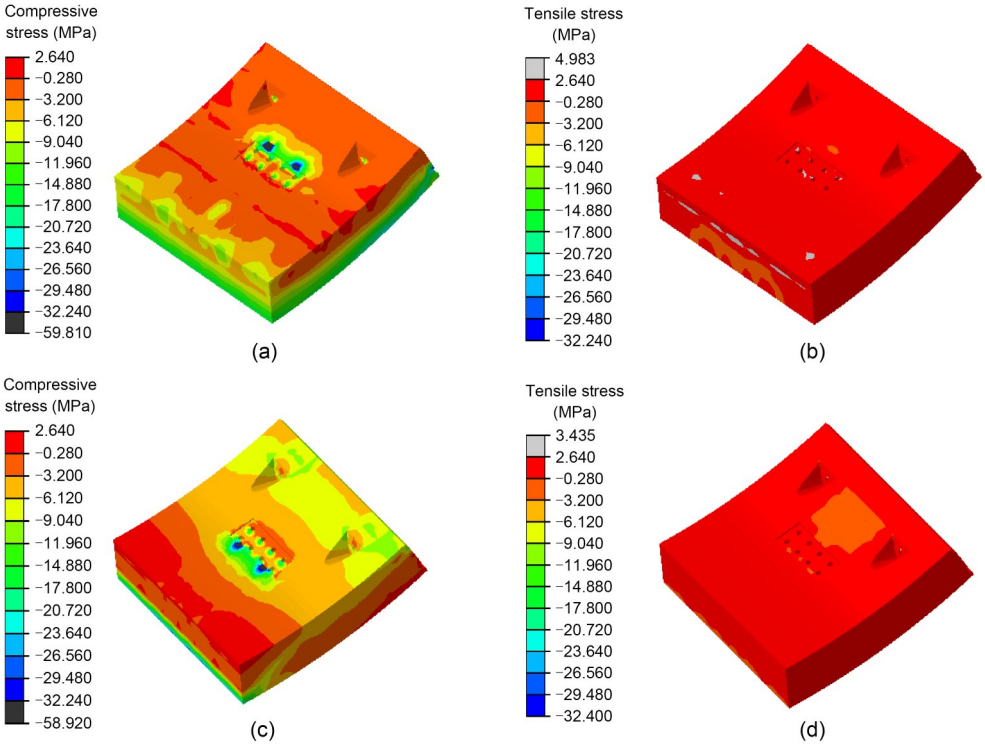

Fig. 20 Damage of concrete around anchor parts: (a) compressive stress, positive bending loading; (b) tensile stress, positive bending loading; (c) compressive stress, negative bending loading; (d) tensile stress, negative bending loading

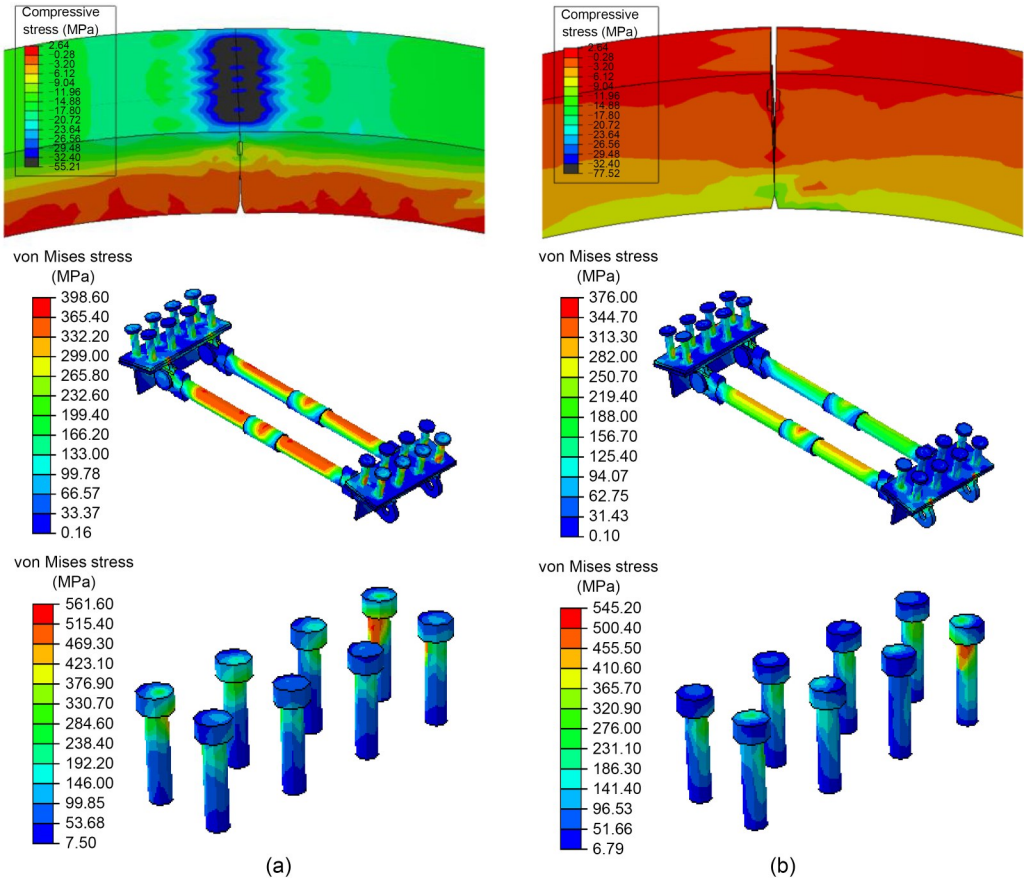

Fig. 21 Stress of concrete, ARSs, anchor parts, and connecting bolts in Model 1 and Model 3 after joint failure (unit: MPa): (a) Model 1, positive bending loading; (b) Model 3, negative bending loading

17 (bending moment of 326 kN·m and axial force of 1640 kN), the joint is open by 8.493 mm and experiences waterproofing failure; meanwhile, both the ARSs and the anchor parts enter the plastic yield state. The stress distribution in the concrete, the ARSs, the anchor parts, and the connecting bolts at the point of joint waterproofing failure is shown in Fig. 21b.

Looking at the numerical results, it is clear that after anchor parts are used to optimize the ARS–concrete connections, the opening of the segmental joint with ARSs is significantly less than the joint without ARSs, under both positive and negative bending loading conditions. This means that ARSs help limit the opening of segmental joints subjected to both positive and negative bending moments. Additionally, with ARSs, the values of positive bending and negative bending moments at the points of failure are both larger than those without ARSs. However, it should be noted that in the case of positive bending loading, the concrete around the anchor parts cracks before the joint failure, and in the case of negative bending loading, it cracks before the joint waterproofing failure. ARSs can be used to strengthen a shield segmental joint when potential opening is a concern and reinforcement is required. ARSs could be particularly useful when only a few joints in the tunnel structures need strengthening, and there is no need to deploy steel plates to reinforce all the lining rings. For shield tunnels which have not yet been constructed, anchor parts can be embedded in the concrete segments in tandem with ARSs to safeguard against potential joint opening. For existing shield lining structures, anchor parts unfortunately cannot be embedded in the concrete segments. In this case, further work would need to be done to optimize the connection between the ARSs and the concrete.

4 Conclusions

Optimized ARSs were developed to strengthen segmental joints in the lining structures of shield tunnels. The installation of ARSs at lining joints is convenient,

as they are easily replaceable and their components can be standardized in production. At the same time, ARSs have the advantage of not covering the lining surface after installation, thereby allowing visual observation of problems with the lining. The deformation and failure characteristics of segmental joints strengthened by ARSs were investigated using full-scale bending experiments and numerical modeling, and an optimization method for ARSs was proposed. A key finding from the experiment was that the amount of joint opening can be limited by ARSs. While an un-strengthened segmental joint failed under the action of positive bending loading with an opening of 5.48 mm, the opening of the strengthened joint was only 1.50 mm under the same loading.

However, ARSs can also separate from the concrete segments during loading if the connection is not designed properly. Thus, numerical modeling was conducted with anchor parts that enhanced the connection between the ARSs and concrete segments. The results showed that an un-strengthened segmental joint failed with an opening of 5.884 mm under the action of a positive bending moment, while the strengthened joint was only opened by 0.228 mm under the same loading. Concordantly, under the action of a negative bending moment, when the opening of the un-strengthened joint was 9.033 mm and the waterproofing failure threshold of 6 mm was significantly exceeded, the strengthened joint was only opened by 2.793 mm under the same loading conditions.

Significantly, it was shown that the failure modes of segmental joints strengthened by ARSs were different under the actions of positive versus negative bending loading. In the case of positive bending loading, first the concrete around the anchor parts cracks, and subsequently the concrete on the external side of the joint crushes. This failure is caused by the crushing of concrete on the external side of the joint, but at the point when the joint is damaged, the amount of opening is still under the waterproofing failure limit. In the case of negative bending loading, the concrete around the anchor parts first cracks, and then the amount of opening exceeds the waterproofing failure limit, i.e., the joint failure is caused by the water leakage.

Acknowledgments

This work is supported by the National Natural Science Foundation of China (No. 52008308), the China Postdoctoral Science Foundation (Nos. BX20200247 and 2021M692447), and the Research Project from Jinan Rail Transit Group Co., Ltd. and China Railway No. 5 Engineering Group Co., Ltd. (No. R2-ZF-2019-039).

Author contributions

Zhiguo YAN: conceptualization; writing–review & editing; funding acquisition. Sihang AI: data curation; software; validation. Xia YANG: supervision; visualization. Long ZHOU: methodology; writing–original draft; funding acquisition. Bing FAN: resources. Huan PANG: investigation.

Conflict of interest

Zhiguo YAN, Sihang AI, Xia YANG, Long ZHOU, Bing FAN, and Huan PANG declare that they have no conflict of interest.

References

Avanaki MJ, Hoseini A, Vahdani S, et al., 2018. Numerical-aided design of fiber reinforced concrete tunnel segment joints subjected to seismic loads. *Construction and Building Materials*, 170:40-54. https://doi.org/10.1016/j.conbuildmat.2018.02.219

Do NA, Dias D, Oreste P, 2014. Three-dimensional numerical simulation of mechanized twin stacked tunnels in soft ground. *Journal of Zhejiang University-SCIENCE A (Applied Physics & Engineering)*, 15(11):896-913. https://doi.org/10.1631/jzus.A1400117

Gong WP, Huang HW, Juang CH, et al., 2015. Improved shield tunnel design methodology incorporating design robustness. *Canadian Geotechnical Journal*, 52(10):1575-1591. https://doi.org/10.1139/cgj-2014-0458

He ZS, Supasit S, Akiyama M, et al., 2020. Life-cycle reliability-based design and reliability updating of reinforced concrete shield tunnels in coastal regions. *Structure and Infrastructure Engineering*, 16(4):726-737. https://doi.org/10.1080/15732479.2019.1674343

Huang HW, Zhang DM, 2016. Resilience analysis of shield tunnel lining under extreme surcharge: characterization and field application. *Tunnelling and Underground Space Technology*, 51:301-312. https://doi.org/10.1016/j.tust.2015.10.044

Huang HW, Shao H, Zhang DM, et al., 2017. Deformational responses of operated shield tunnel to extreme surcharge: a case study. *Structure and Infrastructure Engineering*, 13(3):345-360. https://doi.org/10.1080/15732479.2016.1170156

Jin H, Yu KW, Gong QM, et al., 2018. Load-carrying capability of shield tunnel damaged by shield shell squeezing action during construction. *Thin-Walled Structures*, 132:69-78. https://doi.org/10.1016/j.tws.2018.07.057

Lee WF, Ishihara K, 2010. Forensic diagnosis of a shield tunnel failure. *Engineering Structures*, 32(7):1830-1837. https://doi.org/10.1016/j.engstruct.2010.03.012

Li Z, Liu XZ, Lai HR, et al., 2023. Detailed damage mechanism of deformed shield tunnel linings reinforced by steel plates. *Engineering Failure Analysis*, 143:106850.

https://doi.org/10.1016/j.engfailanal.2022.106850

Liu DJ, Wang F, Zhang DM, et al., 2019. Interfacial stresses of shield tunnel strengthened by a thin plate at inner surface. *Tunnelling and Underground Space Technology*, 91: 103021.
https://doi.org/10.1016/j.tust.2019.103021

Liu DJ, Wang F, Hu QF, et al., 2020. Structural responses and treatments of shield tunnel due to leakage: a case study. *Tunnelling and Underground Space Technology*, 103: 103471.
https://doi.org/10.1016/j.tust.2020.103471

Liu TJ, Chen SW, Lin PQ, et al., 2022. Failure mechanism and strengthening effect of shield tunnel lining reinforced by steel plates with corbels. *European Journal of Environmental and Civil Engineering*, 26(4):1603-1621.
https://doi.org/10.1080/19648189.2020.1717636

Liu X, Jiang ZJ, Zhang LL, 2017. Experimental investigation of the ultimate bearing capacity of deformed segmental tunnel linings strengthened by epoxy-bonded filament wound profiles. *Structure and Infrastructure Engineering*, 13(10):1268-1283.
https://doi.org/10.1080/15732479.2016.1260601

Liu X, Jiang ZJ, Yuan Y, et al., 2018. Numerical investigation of the mechanical behavior of deformed segmental tunnel linings, strengthened by epoxy-bonded filament wound profiles. *Tunnelling and Underground Space Technology*, 78:231-244.
https://doi.org/10.1016/j.tust.2018.04.033

Wang SM, Peng XY, Zhou H, et al., 2023. Deformation control criterion of shield tunnel under lateral relaxation of soft soil. *Frontiers of Structural and Civil Engineering*, 17(5):780-795.
https://doi.org/10.1007/s11709-023-0944-3

Wu B, Ou YL, 2014. Experimental study on tunnel lining joints temporarily strengthened by SMA bolts. *Smart Materials and Structures*, 23(12):125018.
https://doi.org/10.1088/0964-1726/23/12/125018

Wu HN, Xu YS, Shen SL, et al., 2011. Long-term settlement behavior of ground around shield tunnel due to leakage of water in soft deposit of Shanghai. *Frontiers of Architecture and Civil Engineering in China*, 5(2):194-198.
https://doi.org/10.1007/s11709-011-0105-y

Ye XW, Zhang XL, Chen YB, et al., 2024. Prediction of maximum upward displacement of shield tunnel linings during construction using particle swarm optimization-random forest algorithm. *Journal of Zhejiang University-SCIENCE A (Applied Physics & Engineering)*, 25(1):1-17.
https://doi.org/10.1631/jzus.A2300011

Zhai WZ, Chapman D, Zhang DM, et al., 2020. Experimental study on the effectiveness of strengthening over-deformed segmental tunnel lining by steel plates. *Tunnelling and Underground Space Technology*, 104:103530.
https://doi.org/10.1016/j.tust.2020.103530

Zhang JL, Liu X, Ren TY, et al., 2022. Numerical analysis of tunnel segments strengthened by steel–concrete composites. *Underground Space*, 7(6):1115-1124.
https://doi.org/10.1016/j.undsp.2022.02.004

Zhao HL, Liu X, Bao YH, et al., 2016. Simplified nonlinear simulation of shield tunnel lining reinforced by epoxy bonded steel plates. *Tunnelling and Underground Space Technology*, 51:362-371.
https://doi.org/10.1016/j.tust.2015.10.004

Zheng G, Cui T, Cheng XS, et al., 2017. Study of the collapse mechanism of shield tunnels due to the failure of segments in sandy ground. *Engineering Failure Analysis*, 79:464-490.
https://doi.org/10.1016/j.engfailanal.2017.04.030

Zhou C, Ding LY, Skibniewski MJ, et al., 2018. Data based complex network modeling and analysis of shield tunneling performance in metro construction. *Advanced Engineering Informatics*, 38:168-186.
https://doi.org/10.1016/j.aei.2018.06.011

Zhou L, Zhu HH, Shen Y, et al., 2022. Full-scale experimental investigation on progressive failure characteristics of shield segmental lining connected through segmental joints containing ductile-iron joint panels. *Archives of Civil and Mechanical Engineering*, 22(3):120.
https://doi.org/10.1007/s43452-022-00438-0

Zhou L, Shen Y, Guan LX, et al., 2023. Full-scale experiment for segmental linings of deep-buried shield tunnels bearing high inner water pressure: comparison of mechanical behaviors of continuous- and stagger-jointed structures. *Underground Space*, 8:252-266.
https://doi.org/10.1016/j.undsp.2022.03.005